Structure
Article

Improved Structures of Full-Length p97, an AAA ATPase: Implications for Mechanisms of Nucleotide-Dependent Conformational Change

Jason M. Davies,[1,2] Axel T. Brunger,[1,2,3,4,5] and William I. Weis[1,2,*]
[1]Department of Structural Biology
[2]Department of Molecular and Cellular Physiology
[3]Department of Neurology and Neurological Science
[4]Department of Photon Science
Stanford University, Stanford, CA 94305-5432, USA
[5]Howard Hughes Medical Institute, 318 Campus Drive West, Stanford, CA 94305, USA
*Correspondence: bill.weis@stanford.edu
DOI 10.1016/j.str.2008.02.010

SUMMARY

The ATPases associated with various cellular activities (AAA) protein p97 has been implicated in a variety of cellular processes, including endoplasmic reticulum-associated degradation and homotypic membrane fusion. p97 belongs to a subgroup of AAA proteins that contains two nucleotide binding domains, D1 and D2. We determined the crystal structure of D2 at 3.0 Å resolution. This model enabled rerefinement of full-length p97 in different nucleotide states against previously reported low-resolution diffraction data to significantly improved R values and Ramachandran statistics. Although the overall fold remained similar, there are significant improvements, especially around the D2 nucleotide binding site. The rerefinement illustrates the importance of knowledge of high-resolution structures of fragments covering most of the whole molecule. The structures suggest that nucleotide hydrolysis is transformed into larger conformational changes by pushing of one D2 domain by its neighbor in the hexamer, and transmission of nucleotide-state information through the D1-D2 linker to displace the N-terminal, effector binding domain.

INTRODUCTION

p97, also known as valosin-containing protein is a member of the ATPases associated with various cellular activities (AAA) family of proteins (Confalonieri and Duguet, 1995; Neuwald et al., 1999) that transform the chemical energy produced by hydrolysis of ATP into mechanical work needed for a range of cellular processes (Confalonieri and Duguet, 1995; Beyer, 1997; Patel and Latterich, 1998; Vale, 2000). p97 participates in endoplasmic reticulum (ER)-associated degradation (ERAD), in which misfolded proteins are extracted from the ER membrane and directed into proteosomal degradation pathways (Hitchcock et al., 2001; Ye et al., 2001; Rabinovich et al., 2002). In this role, p97 interacts with the Ufd1-Npl4 complex, which in turn can interact with misfolded ER membrane proteins that have been ubiquitinated. p97 has also been implicated in homotypic membrane fusion through its interaction with p47 (Kondo et al., 1997; Uchiyama and Kondo, 2005).

AAA proteins are characterized by the presence of an AAA cassette comprised of ~250 residues containing the Walker A and B nucleotide binding and hydrolysis motifs. A subset of these proteins also contains a second region of homology (SRH) (Lupas and Martin, 2002). The AAA family is further divided into types I and II based on the number of AAA cassettes per protein, with one or two, respectively (Ogura and Wilkinson, 2001). Under physiologic conditions, AAA proteins typically form oligomeric rings containing five or six protomers.

p97 forms a hexameric ring, with each protomer containing an N-terminal (N) domain and two AAA domains, designated D1 and D2 (Peters et al., 1992; Confalonieri and Duguet, 1995; Hanson et al., 1997; Fleming et al., 1998; Rockel et al., 1999). The N domain is a double Ψ-β barrel, and has been shown to interact with a variety of effector molecules, including p47 and Ufd1/Npl4. Interaction with particular adaptor molecules is thought to direct p97 into a particular pathway (Meyer et al., 2000). The two AAA domains, D1 and D2, are each composed of an α/β and an α-helical subdomain. Biochemical studies have established that D2 has the greater ATPase activity of the two, and it has been shown that physiologic p97 activity requires both nucleotide binding and hydrolysis by D2. The role of the hydrolytic activity of D1 is less clear. Nucleotide binding by D1 hastens hexamerization of the complex, but its ATPase activity is not necessary for this process to take place (Wang et al., 2003a). D1 may contribute additional functionality at high temperatures and shows increased hydrolysis activity under heat shock conditions (Song et al., 2003; Wang et al., 2003b). The significance of these differing ATPase activities is uncertain in light of the fact that, in a number of AAA proteins, including p97, binding of adaptor proteins can dramatically impact hydrolysis rates. Indeed, this observation suggests intimate communication between substrate binding and nucleotide hydrolysis, which likely reflects the coupling of hydrolysis and molecular motion required to carry out work on substrates.

A number of structural studies of p97, including X-ray crystallography (Zhang et al., 2000; DeLaBarre and Brunger, 2003, 2005; Huyton et al., 2003; Dreveny et al., 2004), cryoelectron

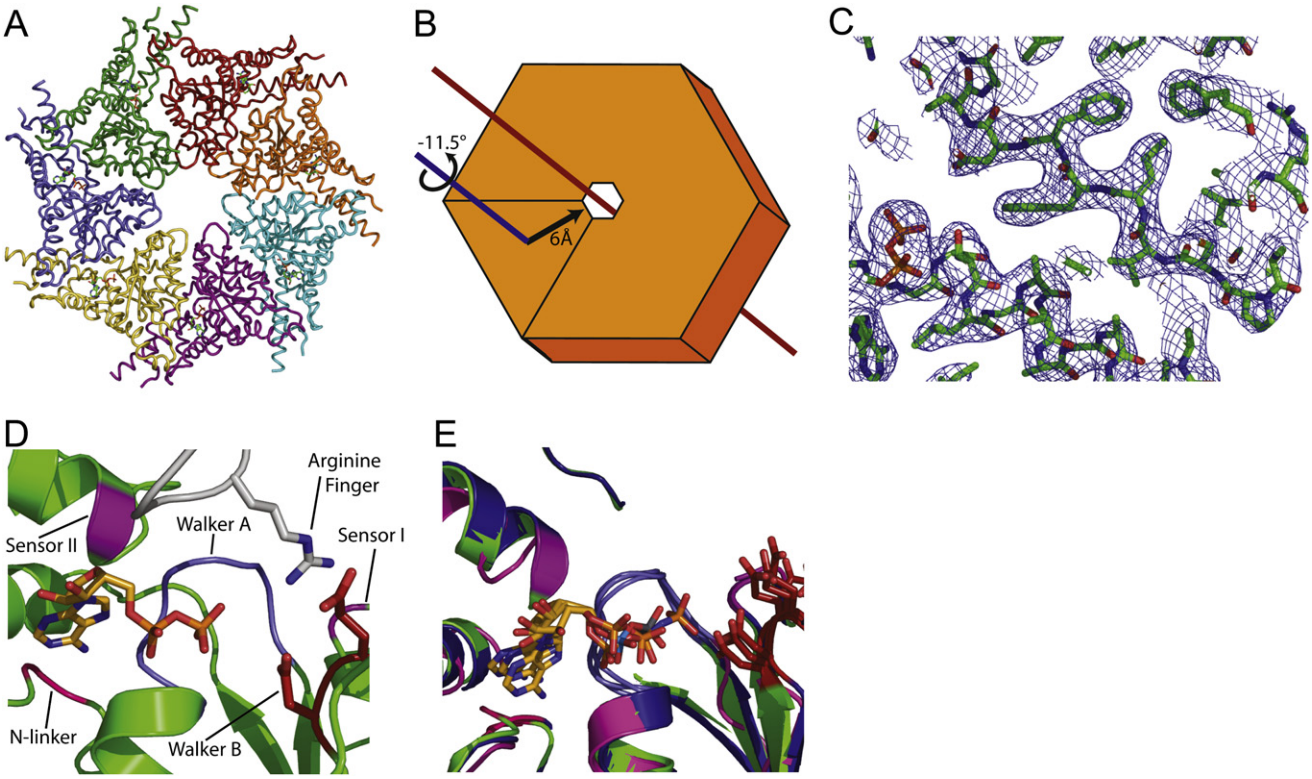

Figure 1. Structure of p97 D2 at 3.0 Å Resolution

(A) The heptameric state of p97 D2 is shown as crystallized. Protomers are uniquely colored.

(B) Schematic of transformations mapping D2 protomer from hepatmer to hexamer. The transformation consists of a 6 Å axial shift accompanied by an 11.4° counter-clockwise rotation about an axis parallel to the molecular 6-fold axis, resulting in relative preservation of the interdomain interface.

(C) Representative electron density of 14-fold averaged D2 domain.

(D) The conformation of the nucleotide binding site of D2 fragment is shown with characteristic AAA motifs highlighted as follows: Walker A (slate); Walker B (red); sensor 1 (purple); sensor 2 (purple); arginine finger (white); N-linker (pink).

(E) The D2 binding sites of the full-length models are superposed for the ATP (magenta), ADP-AlF$_x$ (blue), and ADP (green) state with ADP shown bound in the pocket.

microscopy (Rouiller et al., 2000, 2002; Beuron et al., 2003), and small-angle X-ray scattering (SAXS) (Davies et al., 2005) have been performed in order to understand the coupling of ATPase activity to conformational changes needed to effect function. Among these are EM and SAXS reconstructions of the full-length complex in four nucleotide states (no nucleotide [NN], ATP, the hydrolysis transition state mimic ADP-AlF$_x$, and ADP) that have helped to characterize the global conformational changes of p97 as it progresses through the hydrolysis cycle. Low-resolution (4.7–3.5 Å) crystal structures of the full-length protein grown in the presence of different nucleotides have also been reported (DeLaBarre and Brunger, 2003, 2005; Huyton et al., 2003; Dreveny et al., 2004). The crystal structures of full-length p97 in the ADP-AlF$_x$ and ADP states are unique in that they represent the only structures to date of tandem-domain AAA proteins in their native hexameric state (DeLaBarre and Brunger, 2003, 2005).

Interpretation of the EM, SAXS, and low-resolution crystal data depended on the availability of high-resolution crystal structures of the individual domains. A 2.9 Å structure of N-D1 is available (Zhang et al., 2000). Because of the homology of D1 and D2, the D1 model was used to model the D2 domain in the EM, SAXS, and low-resolution crystallographic work. However, starting from a D2 homology model, the low-resolution crystallographic refinement produced poor Ramachandran statistics and secondary structure definition (DeLaBarre and Brunger, 2003, 2005).

In order to obtain a reliable, high-quality atomic model of an active AAA domain of type II AAA proteins, we have crystallized and determined the structure of the p97 D2 domain at 3.0 Å resolution in a crystal form with high noncrystallographic symmetry. This model was then used in conjunction with improved refinement methods (DeLaBarre and Brunger, 2006; Brunger, 2007) to rerefine the models of full-length p97 in three nucleotide states, ATP, transition state, and ADP. We present here dramatically improved models of full-length p97 that lend new insight into the coupling of nucleotide hydrolysis and force transduction.

RESULTS AND DISCUSSION

Structure Determination of p97-D2 Domain

The p97 D2 region, residues 461–806, was purified and crystallized, and the structure was determined by molecular replacement. The crystal asymmetric unit contains 14 identical copies of the D2 domain arranged in two stacked heptameric rings

(Figure 1A). Several recent reports have found heptamers formed by isolated AAA domains that were previously known to be hexameric in the context of the full-length protein; minimal disruption of domain interfaces is required to change from a 6-fold to a 7-fold symmetric ring (Lee et al., 2003; Rosenberg et al., 2005, 2006). Comparing the heptamer with previously observed hexameric ring structures of p97, the D2 protomers exhibit an outward radial shift of about 6 Å, with rotations around axes perpendicular and parallel to the 7-fold of 0.4° and −11.5°, respectively (Figure 1B). The interprotomer interfaces are virtually identical in the hexamer and heptamer.

The structure was refined at 3.0 Å resolution with strict 14-fold noncrystallographic symmetry imposed, resulting in R_{work} and R_{free} values of 24.4% and 26.2%, respectively, with greatly improved geometry over existing models of this domain (Figure 1C and Table 1). The refined model consists of residues 463–707 and 728–763. Electron density was not well defined for the first two and last 42 residues, as well as the loop from 708 to 727. Despite efforts to crystallize in the presence of, or exchange in, various other adenine nucleotides at 10 mM concentration, the nucleotide binding site in all cases was observed to contain only ADP.

Comparison of the new p97-D2 model with the previously published structures of the D2 domain within the full-length p97 (DeLaBarre and Brunger, 2003, 2005) demonstrates a greater degree of structural homology to D1 than previously reported. Correction of a number of register shifts in the original D2 models improved agreement with secondary structural elements predicted from primary structure alignments with p97 D1 and other closely related AAA proteins. It should be noted, however, that the original work made conservative use of homology modeling for the D2 domain, so most of the large deviations occurred during interpretation and refinement of low-resolution electron density maps. Interestingly, the register shifts occurred in several instances despite the presence of Met residues that were originally replaced with selenomethionine to phase the full-length p97 structure. The methionine sulfur positions in the new D2 model are relatively well preserved, despite changes in backbone arrangement (Figures 2A and 2B). One region where register shifts are particularly vital is the nucleotide binding site, which has been extensively remodeled. Figure 1D shows the revised positions of key binding site residues conserved among AAA proteins.

Table 1. p97 D2 Data and Refinement Statistics

	Native (ADP)
Data collection	
Space group	C2
Cell dimensions	
a (Å)	173.3
b (Å)	167.2
c (Å)	209.5
β (deg)	112.3
Resolution range (Å)	30–3.0
Total reflections	796,409
Unique reflections	108,870
Completeness (%) (last shell)	98.1 (99.3)
R_{merge} (%) (last shell)[a]	8.6 (55.7)
I/σI (last shell)	11.4 (1.5)
Refinement	
Resolution range	50–3.0
R_{work} (%)[b]	24.4
R_{free} (%)[c]	26.2
No. of reflections	
For refinement	96,556
For R_{free} calculation	9759
Total number of atoms in refinement	31,192
Bulk solvent probe/shrink (Å)	1.11/0.90
Bulk solvent level ($e^-/Å^3$)	0.33
Bulk solvent B-factor ($Å^2$)	75.4
Δ_{bonds} (Å)	0.003
Δ_{angles} (deg)	0.732
Average B-factor, all atoms ($Å^2$)	89.7
Crossvalidated σ_A coordinate error (Å)	0.48
Ramachandran analysis (for all residues)[d]	
Most favored region (%)	89.0
Allowed region (%)	11.0
Generously allowed region (%)	0.0
Disallowed region (%)	0.0

[a] $R_{merge} = \Sigma_{hkl} \Sigma_i |I_i(hkl) - \langle I(hkl) \rangle| / \Sigma_{hkl} \Sigma_i I_i(hkl)$.
[b] $R_{work} = \Sigma_{hkl}(|F_o| - k|F_c|)/\Sigma_{hkl}|F_o|$ for reflections in R_{work} set.
[c] R_{free} is computed from a random selection of reflections in the asymmetric unit that was not used during refinement.
[d] As defined by the criteria of Procheck (Laskowski et al., 1993).

Structure Determination of Full-Length p97

The revised model of D2 (3.0 Å resolution) in conjunction with the previously published ND1 model (PDB ID: 1E32; 2.9 Å resolution) were used as starting models for rerefinement against the low-resolution structure factors for full-length p97 in three nucleotide states, ATP (from PDB ID: 1YPW; 3.5 Å resolution), ADP-AlF_x (from PDB ID: 1YQ0; 4.5 Å resolution), and ADP (from PDB ID: 1YQI; 4.25 Å resolution) (DeLaBarre and Brunger, 2003, 2005). Although only a few additional residues were added to the models, the revised full-length models show significant improvement in secondary structure geometry, R values (Table 2), and real-space R values (Figure 3).

The availability of a reliable D2 structure was essential to obtain these improved structures, since the electron density maps derived from the previously published models were poorly defined in several regions (e.g., Figures 2A and 2C). A number of parameters were important for these low-resolution refinements. In particular, we reran a series of trials to find optimal parameters for noncrystallographic symmetry, refinement target, bulk solvent correction, and B-factor sharpening.

Noncrystallographic Symmetry

The factor that most improved model quality, as assessed by minimizing R_{free}, was proper definition of noncrystallographic symmetry. Each of the three nucleotide-bound states was initially refined with strict noncrystallographic symmetry imposed, and, when no further drop in R values was observed, various reductions in symmetry were examined. The previous structures were refined with a tight restraint scheme that excluded residues in crystal packing interfaces and divided the protomers

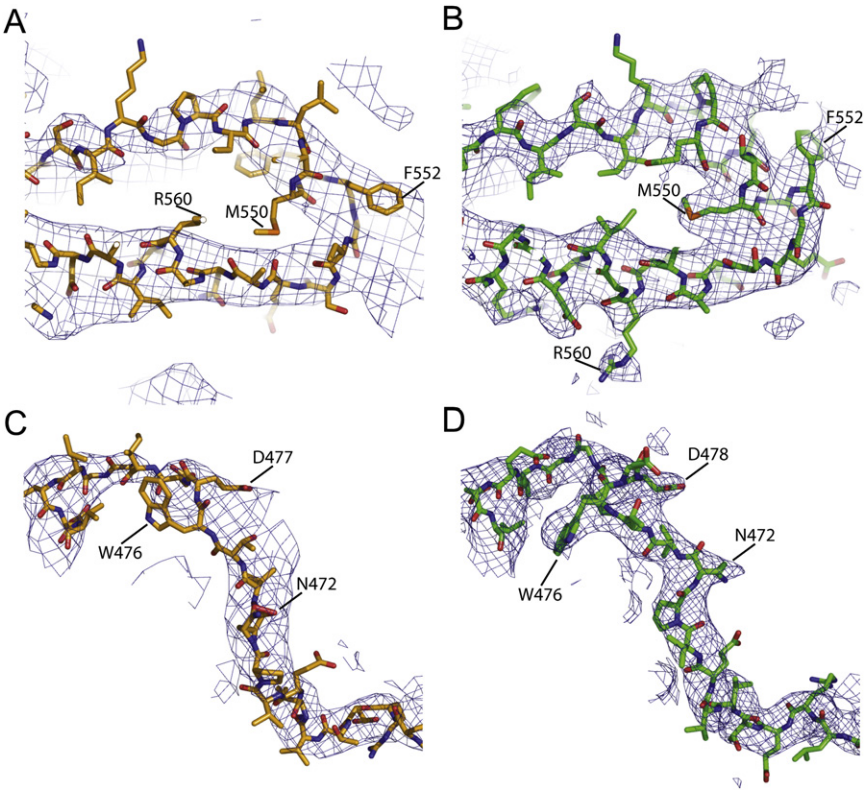

Figure 2. A Series of Trials Were Performed to Obtain Optimal Model Refinement Parameters for Noncrystallographic Symmetry, Refinement Target, Bulk Solvent Correction, and B-Factor Sharpening

Phase combined, σ_A-weighted $2F_o - F_c$ maps were calculated for the ADP-AlF$_x$ diffraction data with either (A and C) the final model and refinement parameters from 1YQO or (B and D) the new ADP-AlFx model with MLHL refinement target, modified bulk solvent correction as implemented in CNS 1.2, and optimized B-factor sharpening, as determined with the sharpen.inp script included with CNS 1.2. All maps are shown with electron density at 1σ. (A and B) A loop in D2, residues 530–570. Note that, although the backbone position of M550 is shifted in the new models, the relative position of the sulfur is preserved, in agreement with experimental seleno-methionine data. (C and D) The D1-D2 linker region, residues 460–480. Note the difference in improvement in electron density, particularly at the C terminus, allowing for more accurate placement of side chains.

into subdomains (DeLaBarre and Brunger, 2003, 2005). This allows rigid-body motion of the domains without variations in internal domain geometry. This same scheme was adopted in the rerefinement for the ADP and ADP-AlF$_x$ states on the basis of giving the lowest R_{free} value. In agreement with previous work, the ADP state showed the greatest deviation from strict symmetry, with relative motion of the three domains between protomers observed on the same scale as what was previously reported (DeLaBarre and Brunger, 2003, 2005). In contrast, the ADP-AlF$_x$ state exhibited much less variability in the positions of domains within the protomers, again in agreement with previous work, with notable differences in the nucleotide binding site, as is discussed below. The ATP state exhibited strict noncrystallographic symmetry, as was previously reported (although it was previously treated with NCS restraints rather than NCS constraints; cf. Figures 3C and 3F).

Refinement Target

Although the rerefinement was carried out with models derived from higher-resolution crystal structures, tests were performed to reassess if the addition of low-resolution experimental-phase information might significantly improve map quality, as was done in the previously published structures. Two refinement targets were assessed: MLF (without phase information) and MLHL (with experimental phase information). R values were only minimally impacted by the choice of refinement target. Electron density maps generated for each nucleotide state with and without experimental phases were analyzed for differences. Most regions of the structures showed only very minor differences in electron density, primarily at the distal portions of long side chains. However, in areas that are poorly defined, such as in the D1-D2 linker region and the D2 α-helical domain of the ATP state, the addition of experimental-phase information improved map quality more significantly (Figure 2). For that reason, experimental-phase information was included in the rerefinement of all nucleotide states.

Bulk Solvent Correction and Other Improvements of Refinement Methodology

Refinement was carried out with CNS version 1.2 (Brunger et al., 1998; Brunger, 2007). One of the most significant improvements in version 1.2 is a revised method for bulk solvent correction that is particularly beneficial for crystal structures of 3.0 Å resolution or lower. The bulk solvent procedure in the earlier versions of CNS often resulted in numerical instabilities for the refinement of the solvent parameters, k_{sol} and B_{sol}, for structures determined at low to moderate resolution (i.e., lower than 3 Å). In version 1.2, a grid search for k_{sol} is performed while determining B_{sol} by least-squares refinement for each selected value of k_{sol}. A more detailed description of these and other improvements (such as the the handling of overall anisotropic thermal factor scaling) in version 1.2 of CNS can be found in the work by Brunger (2007). Holding all refinement parameters constant, positional and grouped B-factor minimization with version 1.2 resulted in an improvement in R_{work} and R_{free} of about 2% compared with identical treatment with version 1.1.

B-Factor Sharpening

B-factor sharpening was applied to the previously published full-length p97 structures in the ADP and ADP-AlF$_x$ states, with good results (DeLaBarre and Brunger, 2003, 2005). For the rerefined structures, the improvements upon B-factor sharpening are even more pronounced, more clearly defining side chains (compare

Table 2. p97 Full-Length Refinement Statistics

Structure	Full-Length ATP	Full-Length ADP-AlF$_3$	Full-Length ADP
Resolution range	30–3.5	30–4.4	40–4.25
R_{work} (%)[a]	27.1	22.9	19.8
R_{free} (%)[b]	28.5	28.6	22.6
Number of reflections			
For refinement	91,879	43,565	51,285
For R_{free} calculation	4798	3062	4091
Total number of atoms in refinement	5,229	17,151	17,139
Bulk solvent probe/shrink (Å)	0.5/0.5	1.0/1.0	1.0/1.0
Bulk solvent level (e^-/Å^3)	0.25	0.30	0.30
Bulk solvent B-factor (Å^2)	53.1	179.2	154.3
Δ_{bonds} (Å)	0.007	0.007	0.008
Δ_{angles} (deg)	1.33	1.37	1.37
Average B-factor all atoms (Å^2)	147.8	248.8	206.9
Crossvalidated σ_A coordinate error (Å)	1.15	1.38	1.04
NCS rmsd relative to the A chain			
B chain	—	0.660	0.632
C chain	—	0.603	0.619
Ramachandran analysis (for all residues)[c]			
Most favored region (%)	70.8	72.3	81.3
Allowed region (%)	28.1	27.5	17.6
Generously allowed region (%)	1.1	0.2	0.9
Disallowed region (%)	0.0	0.0	0.2

[a] $R_{work} = \Sigma_{hkl}(|F_o| - k|F_c|)/\Sigma_{hkl}|F_o|$ for reflections in R_{work} set.
[b] R_{free} is computed from a random selection of reflections in the asymmetric unit that was not used during refinement.
[c] As defined by the criteria of Procheck (Laskowski et al., 1993).

Figure 2A [old model] and Figure 2B [rerefined model]). The regions that showed the most improvement in density were those that were less well defined, such as the D1-D2 linker region (Figures 2C and 2D). Inspection of the B-sharpened maps did not reveal any regions that were significantly degraded relative to the non-sharpened maps, so B-factor sharpening was maintained for building.

Comparison of Rerefined Full-Length p97 Structures with Published Models

The overall fold of full-length p97 is unchanged upon rerefinement. There are, however, many differences in detail, including several register shifts, which produce overall rmsd values of 3.2 and 3.4 Å for Ca atoms for the ADP and ADP-AlF$_x$ states, respectively. Many of the more significant differences between rerefined and previous models reside in the D2 nucleotide binding site. In previous models of the site, conserved chemical features were placed in significantly different positions in each nucleotide state. For instance, the adenine rings in previous models occupied substantially different portions of the binding pocket, resulting in variable contacts between the ring and the surrounding protein, and discrepant positions for the surrounding residues among the states. These models suggested a mechanism for nucleotide state sensing involving the adenine ring, as opposed to the presence or absence of bound γ-phosphate. In contrast, the conformation of the nucleotide and contacts made with the adenine ring in the present models remain relatively unchanged across nucleotide states (Figure 1E). Such a conserved base binding pocket is consistent with models of other AAA binding sites that have been solved in multiple nucleotide states (Sousa et al., 2000; Wang et al., 2001; Niwa et al., 2002; Gai et al., 2004), and is consistent with nucleotide state sensing occurring primarily at the terminal phosphate position.

The ATP-bound p97 crystal diffracted to the highest resolution (3.5 Å) of the full-length crystals, but even with 4-fold NCS averaging, the maps for this state are poorly defined in certain areas, the most significant of which is the D2 α-helical domain. As with previous models of the ATP and the NN states, much of the D2 α-helical subdomain is missing in the present model, although the enhanced low-resolution refinement procedures helped clarify several areas of poorer definition, such as the D1-D2 linker region. The D2 α/β domain in general, and, in particular, the nucleotide binding site are well defined. When compared with other nucleotide states there are significant differences within the nucleotide binding site in the positions of key residues with direct implications for the mechanism of hydrolysis, as discussed below.

The ADP and ADP-AlF$_x$ crystals are each composed of three nonidentical protomers per asymmetric unit. In the previous ADP-AlF$_x$ model, the AlF$_x$ moiety was fully occupied in only one out of three D2 protomers, but, upon rerefinement with identical symmetry restraints, the nucleotide was found to be present in all copies with occupancies near 1. Although the nucleotide state and binding site configuration were found to be the same from one protomer to the next, the relative arrangement of domains differed among protomers in both crystals.

The relative positions of the N, D1, and D2 domains can be described by defining two vectors with a common origin at the ribose C3* of the bound nucleotide in D1 and extending to defined positions in N (carbonyl carbon of residue 107) and D2 (ribose C3* of the bound nucleotide) (Figure 4). Since the N-D1 and D1-D2 distances remain relatively invariant across nucleotide states, the magnitude of rigid-body domain changes can be coarsely quantified by calculating the N-D1-D2 angle for protomers in each state. The ATP state was refined with strict 4-fold NCS, so all four copies in the asymmetric unit have an N-D1-D2 angle of 108.4°. The ADP-AlF$_x$ crystals had N-D1-D2 angles ranging from 99.5° to 103.9°, and ADP crystals had angles ranging from 97.1° to 103.0°. The angles for the latter two states imply a certain degree of interdomain flexibility that is independent of nucleotide state.

There are three key regions in the central pore that are required for ERAD activity, but which are not directly related to ATPase activity (DeLaBarre et al., 2006). Resides R586 and R599 are located on a loop at the entrance to the D2 pore, and have been proposed to participate in the denaturing of substrate proteins. Residues F551 and Y552 form a hydrophobic surface on a loop within the D2 pore. Residue H317 is located at the

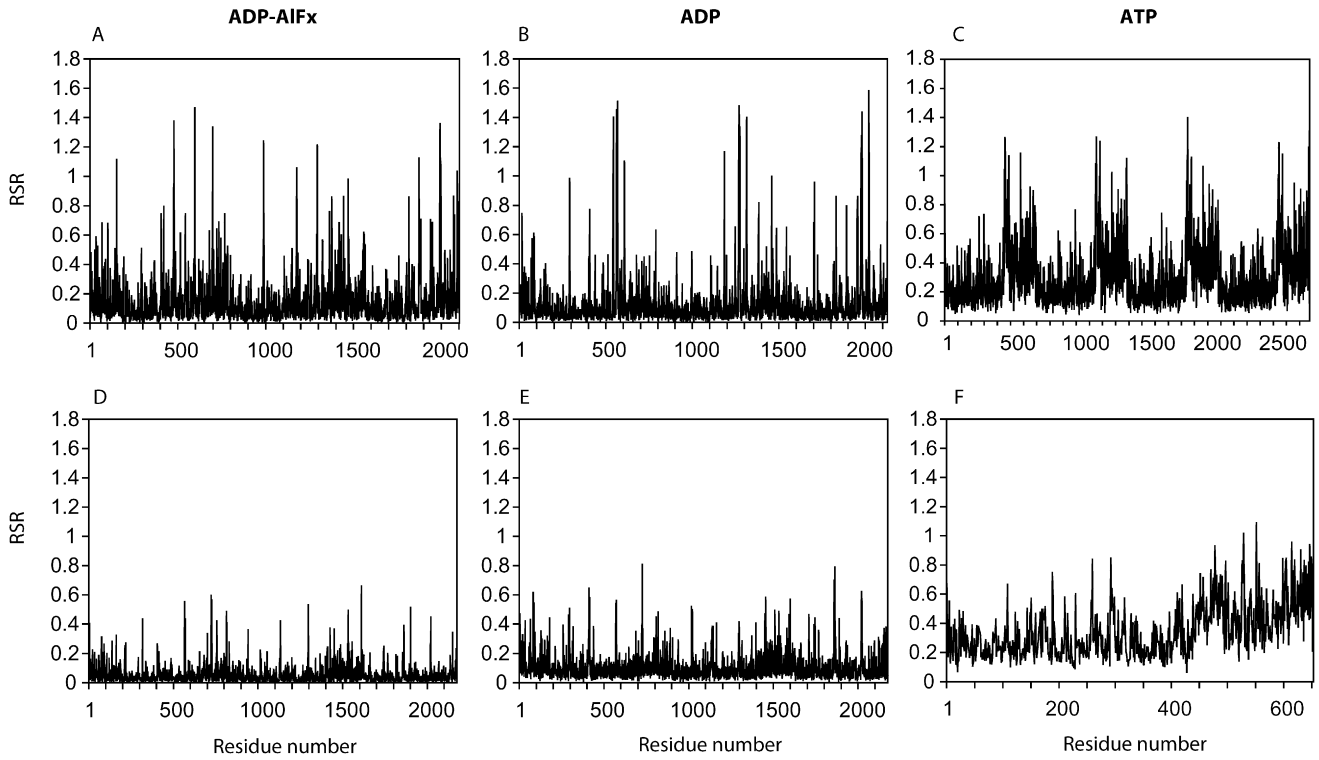

Figure 3. Real-Space R Values

Real-space R values plotted from the original (A–C) and rerefined (D–F) full-length p97 structures. (A and D) ADP-AlFx; (B and E) ADP; (C and F) AMP-PNP.

entrance to the D1 pore, and represents the most constricted portion of the channel.

Analysis of pore residues in the various states of the ATP hydrolysis cycle reveals that the positions of D2 residues are relatively constant between the ADP and ADP-AlF_x states, with the hydrophobic residues 551/552 clustering tightly on the solvent-exposed portion of the loop (Figures 5A and 5B). However, binding of ATP results in a large-scale reorientation of the D2 α/β domain. The shift displaces R599 by approximately 7 Å and is accompanied by disordering of the portion of the loop surrounding R586. The tip of the hydrophobic loop flips up toward D1 such that the hydrophobic residues are buried in the D1-D2 interface. There is an interaction between synaptotagmin I (SytI) and p97 that involves binding to K565, which is also in the D1-D2 interface (DeLaBarre et al., 2006). Remodeling of the hydrophobic residues in the ATP state places Y551 within 6.5 Å of K565, so rearrangement of the loop in this state might serve to preclude binding to SytI through this residue. H317 has been proposed to coordinate a zinc molecule in previous models of full-length p97 (DeLaBarre et al., 2006). Electron density is still found in the center of the D1 pore in the revised structure of the ADP state. However, the limited resolution of the data does not allow a chemically plausible model of the putative zinc coordination by H317.

Differences between D1 and D2 Binding Sites

Biochemical and structural data suggest that the D1 and D2 ATPases have different intrinsic activity levels, with D1 essentially inactive under physiologic conditions, but capable of becoming active under heat shock conditions. Comparison of the D1 and D2 nucleotide binding sites reveals structural differences that account for their respective activities.

Sensor I Loop Position

As described below, the D2 sensor I region appears to be centrally involved in generating the conformational changes associated with hydrolysis, as the sensor asparagine (N348 in D1, N624 in D2) shifts to interact with the ATP γ-phosphate. These changes produce large-scale domain movements at the periphery of the protomer though a lever arm mechanism. Differences in this region of D1 might help explain the differences in hydrolytic activity. Comparison of the D1 and D2 sensor I regions reveals that the loop on which the sensor asparagine resides is shifted away from the bound nucleotide in D1 by ~2 Å (Figure 6A), which effectively prohibits interaction of D1 sensor I N348 with nucleotide. In D2, this loop is flanked by an α helix from the C-terminal tail region. The side of the helix that faces the sensor I loop contains several bulky side chains that interact with the sensor loop to "push" it toward the nucleotide binding site and into position to interact with the γ-phosphate. In contrast, this helix is absent in D1, and the loop instead adopts a conformation that is incompatible with nucleotide sensing. The observation that D1 exhibits hydrolytic activity at high temperature (Song et al., 2003) could be explained by increased D1 loop motion under conditions of higher thermal energy, driving interaction of sensor I with the nucleotide.

Arginine Finger

Visual inspection of the nucleotide binding pockets for D1 and D2 revealed that the D1 pocket is markedly smaller than the

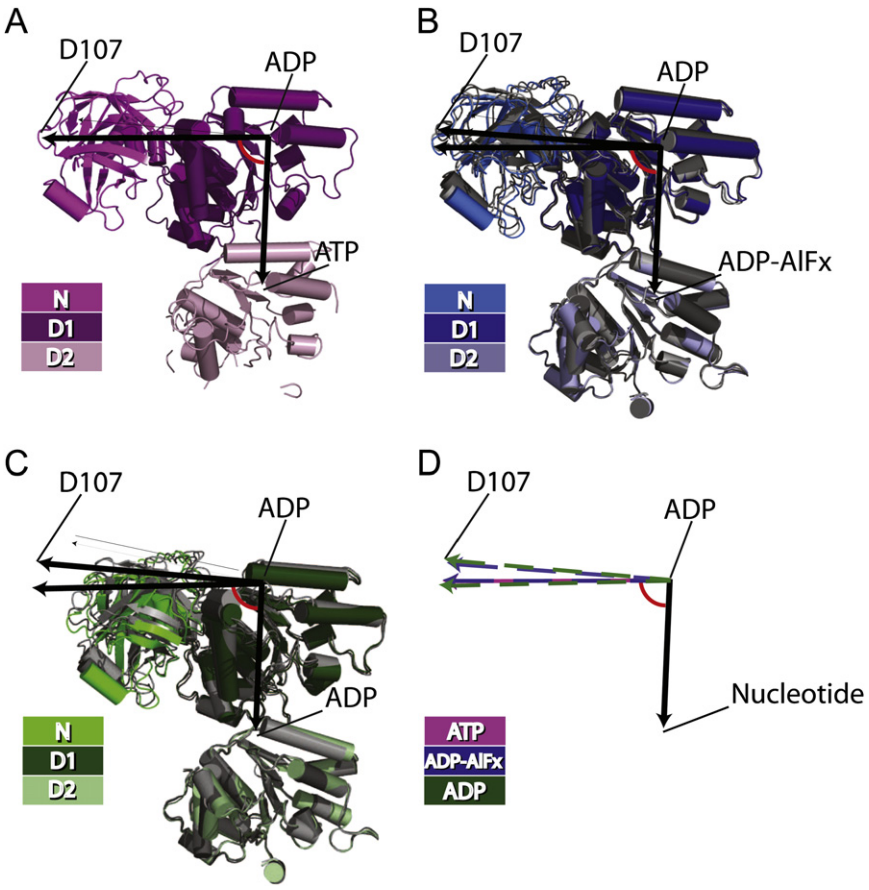

Figure 4. Domain Motions of p97 through the Hydrolysis Cycle

The relative position of the N, D1, and D2 domains are shown by vectors drawn from the ribose C3* atom of the bound ADP in D1 to the Cα atom of residue 107 of the N domain, and to the ribose C3* of the bound nucleotide in D2. (A) ATP, magenta; (B) ADP-AlFx, blue; (C) ADP, green. In each panel, the N domain has an intermediate shade, D1 a dark shade, and D2 a light shade. In (B) and (C), the D1 and D2 α/β subdomains of the independent copies in the asymmetric unit have been superimposed; one protomer is shown in color, and the others in gray. (D) Vectors obtained after superposition of the D1 α/β subdomain of the crystallographically unique protomers within the asymmetric unit of the different nucleotide states, colored as in (A–C). The D1-D2 vectors are overlaid to show the relative displacement of the N domains.

D2 domain in each nucleotide-bound state. The binding site is located in the interprotomer interface and contains residues from two adjacent protomers. In particular, the conserved AAA motifs are localized to one protomer, with the exception of the "arginine finger," which is contributed by the adjacent protomer. The binding site elements contributed by the nonarginine finger regions are relatively invariant between D1 and D2, but the proximity and angle of interaction of the adjacent protomer bearing the arginine finger changes significantly. One means of quantifying the size difference between domains is to compare the distances from arginine finger to terminal phosphate for each state and domain (Figures 6B and 6C). The nucleotide binding site for D1 of each state is essentially constant, with an arginine-to-β-phosphate distance of ~2.9 Å. The distances for the D2 domain range from 4.2–6.6 Å. Likewise, the distance from arginine finger to sensor I is reduced from 6.3–6.8 Å in D2 to 4.4 Å in D1. These distances serve as surrogates for volume of the binding pocket, and confirm the visual impression that D1 has a significantly smaller binding pocket. The smaller pocket might disfavor triphosphate binding and thereby increase the relative affinity for ADP. At higher temperatures, increased mobility of elements surrounding the binding site, including the sensor I loop, could "open" the binding site to allow for more free exchange of nucleotide and for active hydrolysis. One corollary of smaller binding pockets in D1 is that the D1 ring is more constricted than D2, which is reflected in its smaller pore diameter.

Differences among Nucleotide States

Nucleotide Binding Sites

Superposition of the three rerefined models reveals changes in the nucleotide binding sites and relative domain arrangements that might be attributed to progression through the nucleotide hydrolysis cycle. All previous crystal structures of p97 show ADP bound to D1 (Zhang et al., 2000; DeLaBarre and Brunger, 2003, 2005; Huyton et al., 2003; Dreveny et al., 2004), a finding supported by several biochemical studies. Increased tryptophan fluorescence occurred only with addition of nucleotide to the D2 domain, with no changes observed resulting from D1 domain binding (Wang et al., 2003a). Moreover, only half of the 12 sites are available for binding to ADP by isothermal titration calorimetry (DeLaBarre and Brunger, 2003). Finally, HPLC analysis of urea-denatured full-length p97 showed that six equivalents of ADP are always bound, irrespective of exogenous nucleotide addition (Davies et al., 2005). In agreement with these data, the rerefined models show that the D1 nucleotide binding site remains fully occupied by ADP in all states, and, thus, it is the D2 binding site that shows the greatest diversity of configurations and will be the subject of further analyses.

Sensor I Loop

Analysis of the canonical AAA nucleotide binding site motifs of the D2 domain reveals that the major difference among states is found in the sensor I region (Figures 7A–7C). Electron density for both ADP and ADP-AlF_x states is well defined in proximity of the sensor I residue N624, with the asparagine side chain rotated away from the nucleotide binding site. Maps for the ATP state demonstrate rotation of the N624 side chain into the binding site such that it contacts the ATP γ-phosphate (distance = 3.2 Å). The perturbations caused by this rearrangement have both direct and indirect effects on the subdomain that result in global conformational changes. In the indirect mechanism, the

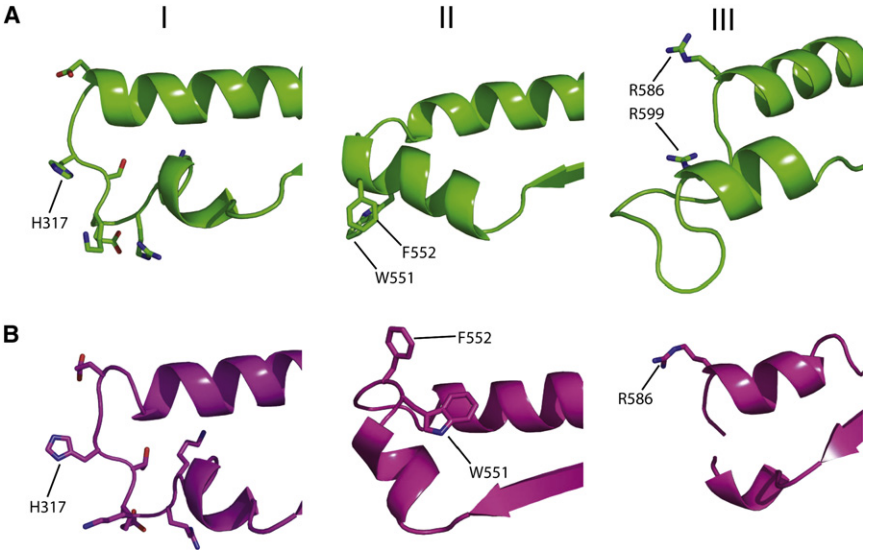

Figure 5. Location of Key Interacting Residues Lining the Pore of p97
(A) ADP state.
(B) AMP-PNP state.
Detailed views of pore loops containing residues H317 (I), W551/F552 (II), and R586/R599 (III).

repositioning of N624 is accompanied by a break in the electron density at T623. Local perturbations are propagated along the length of the β sheet and result in displacement of the distal portions of the subdomain (Figure 7B). The distal loops that exhibit the largest changes, comprised of residues 498–507 and 584–596, are involved in interprotomer interactions with the α-helical and α/β subdomains, respectively, of D2 from the adjacent protomer. The electron density for the D2 α-helical subdomains in the ATP state is much more poorly defined than in the other two nucleotide states, which is likely due to a significant conformational change. The direct effect is mediated by interaction with residues D580 and K584, which form a network of salt bridges in the ADP state (Figure 7C). Rotation of the T624 side chain puts it out of range of interaction with the other two residues, which likely contributes to disordering of the loop 584–596. Both of these effects involve interactions of adjacent D2 domains, so the observed differences between states suggest that global conformational changes are due, at least in part, to D2 domains pushing on their neighbors.

Walker A Motif

The Walker A motif is one of the defining characteristics of AAA proteins, and has been shown to be involved in nucleotide binding and hydrolysis. The D1 and D2 motifs each contain an essential, conserved lysine, K251 and K524, respectively, that interacts with the terminal phosphate groups of the nucleotide and thus serves as a nucleotide state sensor. D1 is effectively inactive and always bound to ADP, and it has been postulated that the D2 nucleotide state is communicated to N via interaction of the D1-D2 linker with D1 (DeLaBarre and Brunger, 2003). The D1-D2 linker consists of residues 461–480. The N- and C-terminal halves of the linker abut the D1 and D2 domains, respectively, near their nucleotide binding sites. The conformation of the linker is relatively invariant at both ends, but the central portion near E470 behaves like a hinge that changes conformation according to nucleotide state (Figure 7D). Comparing the position of K524 across the hydrolysis cycle, local backbone deformations are relatively minimal, but these small displacements are magnified by the lever arm formed by helix 6′ of D2 to result in significant shifts of the residues at the distal tip (Figure 7E). Residue N538 sits at the distal end of the helix and makes contact with the D1-D2 linker at residue E470. As a result, as the nucleotide state changes, so does the conformation of the linker region. In this manner, nucleotide state information is relayed from D2 to distant domains.

Arginine Finger

The arginine finger is a feature common to AAA and other nucleotide triphosphatases. It consists of an arginine residue that protrudes into the nucleotide binding site and has been shown in other systems to be essential for nucleotide hydrolysis by stabilizing the leaving γ-phosphate group. In AAA proteins, the nucleotide binding site is at an interdomain interface, with the arginine finger present on an adjacent protomer. Due to its unique position linking adjacent protomers, it has been the subject of interest in potential interdomain communication of the nucleotide state. A subset of AAA proteins, including p97, DnaA, FtsH, and NSF, have a short insertion into the sequence in this region that results in the presence of two arginine residues separated by two residues, usually Pro-Gly. Each of the two p97 arginines has been proposed to function as the arginine finger based on both sequence homology and structural modeling, thus introducing some ambiguity as to which is the interacting residue.

The higher resolution structure of the isolated p97 D2 domain strongly suggests that R635, not R638, is the arginine finger, as

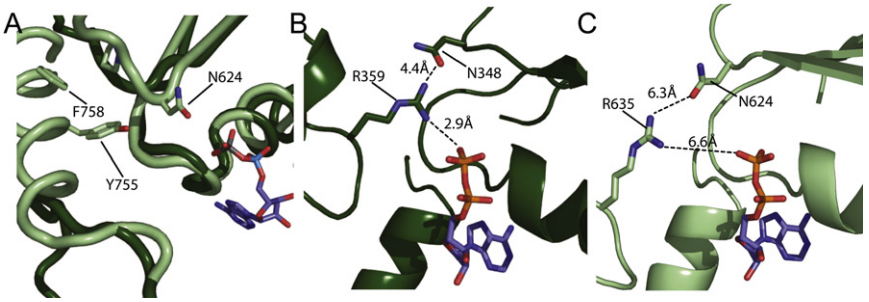

Figure 6. Comparison of Nucleotide Binding Sites in D1 and D2
(A) The nucleotide binding pockets for the D1 (dark green) and D2 (light green) domains are superposed. Note that a helix of the C-terminal region of D2 impinges on the sensor I region of that domain to bring sensor I into proximity of the bound ATP.
(B and C) The sensor I regions of D1 (B) and D2 (C) are shown in the ADP state. Distances of the arginine finger to the ADP β-phosphate and to the sensor I asparagine are indicated.

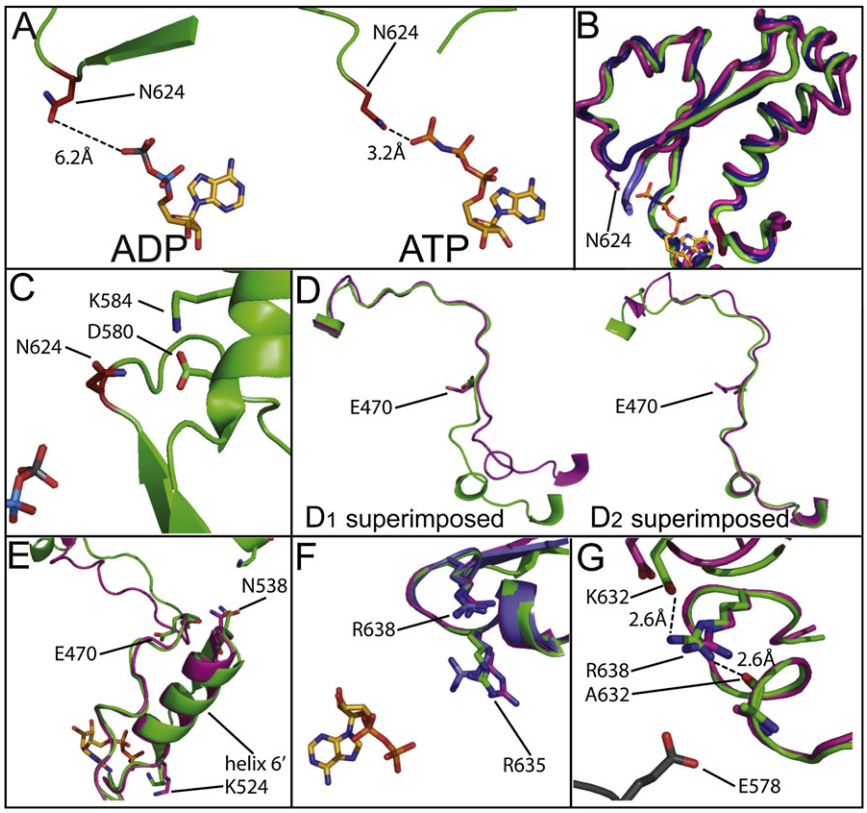

Figure 7. Mechanisms of Transmission of Nucleotide State

(A) Interactions of the sensor I region in the D2 binding site with ADP and AMP-PNP.

(B) Comparison of conformations of β sheets in the presence of ATP (magenta), ADP-AlFx (blue), and ADP (green) in the D2 binding site. Note the propagation of small displacements along the lever arm formed by the sheet, with distal displacements of 3.3 Å.

(C) Stabilization of the α-helical domain by salt bridges linked to sensor I region in the ADP state.

(D) Comparison of conformations of the D1-D2 linker in ATP (magenta), and ADP (green) states when protomers are aligned on the D1 or D2 α/β subdomains. Note the relative rigidity of the proximal and distal portions of the linker region flanking a central hinge.

(E) Comparison of conformations of D2 Walker A (K524) in the presence of ATP (magenta) and ADP (green) with propagation of motions over the helix 6′ lever arm. Details of interactions between N538 and E470 are shown.

(F) Comparison of the positions of potential arginine fingers R635 and R638 in the presence of ATP (magenta), ADP-AlFx (blue), and ADP (green). The ADP bound to the adjacent subunit is shown.

(G) Local and interprotomer interactions of R638 are shown in the ATP (magenta) and ADP (green) states. The adjacent subunit is shown in gray, from the AMP-PNP-bound structure.

it is the only residue that is correctly oriented for contact with the adjacent nucleotide (Figures 1D and 7F). Although it might be argued that the position of these residues are influenced by the heptameric structure, we noted above that the interfaces between protomers in the heptamer and hexamer are almost identical, and the lower-resolution full-length hexamer structures give no indication that this region differs between the heptamer and hexamer. This finding is consistent with the structure of FtsH, which shares the same sequence insertion, in which it was observed that only the first arginine residue was close enough to interact with nucleotide (Suno et al., 2006). The rerefined models of full-length p97 presented here have average distal phosphate-to-arginine finger distances of ~3.4 Å (ATP), ~4.7 Å (ADP-AlF$_x$), and ~6.7 Å (ADP) in the D2 domain (Figure 7F). These values are well within the 3–9 Å range found in previously published models of AAA proteins, and are consistent with a role in stabilizing the leaving group. In contrast to previous models, the arginine side chain in each state points toward the nucleotide binding site, and the arginine occupies a consistent position within the site (Figure 7F). Likewise, large displacements are not observed in adjacent residues, which might argue against a role for the arginine finger in interdomain communication, although this cannot be formally excluded given the limited range of motion observed between states.

The position of R638 makes it unlikely to behave as the arginine finger, which raises the question of its true role in p97. Mutation of R638 decreases p97 ATPase activity 100-fold, but it does not impact cooperativity (DeLaBarre et al., 2006). Interestingly, mutation of the homologous residue in FtsH likewise abolishes ATPase activity (Karata et al., 1999), whereas mutation in NSF eliminates SNARE disassembly without impacting hydrolysis (Matveeva et al., 2002). Thus, it appears that there is not a unifying functional role played by this SRH arginine. Nevertheless, the present models give clues as to its role in p97. R635 and R638 both occupy a loop that sits at the interprotomer interface. Although R638 does not interact with the adjacent nucleotide directly, it interacts with the carbonyl oxygen of A632 (2.6 Å) and the side chain of D609 of the adjacent protomer (2.6 Å) (Figure 7G). There is also a shared interaction between E578 of the adjacent protomer and both R635 and R638. As the molecule progresses through the hydrolysis cycle, the relative distances vary, shifting the acidic residue away from R635 toward R638 as it proceeds from ATP (5.5 Å) to ADP (3.4 Å). These contacts likely help to position R635 within the binding pocket such that it can participate in hydrolysis. Thus, mutation of R638 would adversely impact hydrolysis indirectly through misalignment of R635 within the binding site.

Domain Arrangements

Superposition of the D1 α/β subdomain from each nucleotide state allows for analysis of relative domain displacements between states (Figures 4A–4D). The rerefinement essentially confirms conclusions drawn in the previous study (DeLaBarre and Brunger, 2005). The maximum observed inter-state change in the N-D1-D2 angle is on the order of 11°, which is similar to the values noted for same-state interprotomer displacements (ADP and ADP-AlF$_x$). With inter-state and same-state interprotomer displacements on the same order and in the same direction, it is unclear whether differences observed in the full-length p97 crystal structures described here represent changes that occur in solution. Indeed, solution SAXS data have demonstrated

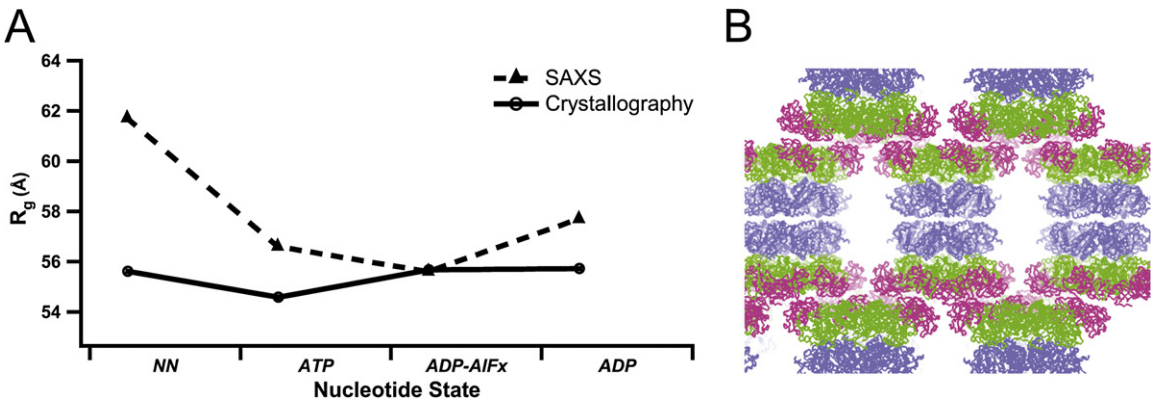

Figure 8. Comparison of SAXS and Crystallographic Models

(A) Comparison R_g in each nucleotide state between models derived from solution scattering (Davies et al., 2005) versus X-ray crystallography.

(B) Crystal contacts of full-length p97. The crystal packing arrangement of full-length p97 is shown to demonstrate the extensive intermolecular crystal contacts, as previously described (DeLaBarre and Brunger, 2003, 2005). Areas of contact are circled at the N-N and D2-D2 interfaces. The ADP state is shown, but all states exhibit similar packing arrangements. Domains are colored as follows: N, pink; D1, green; D2, blue.

conformational changes through the hydrolysis cycle that are both larger in magnitude and sometimes different in direction of change (Davies et al., 2005). Comparison of the radii of gyration (R_g) of models derived from SAXS versus crystallography (Figure 8A) suggest differing pathways through hydrolysis at the gross level, and that the pathway suggested by crystallography might not be indicative of the changes in solution. This discrepancy is probably due to the extensive contacts made by the D2 and N domains with adjacent hexamers in the crystal lattice (Figure 8B). The contacts could limit mobility and trap relatively low-energy, but not necessarily physiologically relevant, conformations in the crystal lattice. Nevertheless, the directions of some of the observed conformational changes in the crystal structures could be similar to those of the larger-scale motions in solution. It should be noted that, although the SAXS data can demonstrate large-scale changes with reasonable certainty, they are limited in that they cannot reveal the nature of small-scale chemical interactions, such as the mechanistic details for which firm evidence exists in the crystal structures.

Conclusions

In this work, we report a number of insights into the mechanism of action of p97 provided by solution of the highest-resolution crystal structure of an active ATPase domain of this AAA subtype and rerefinement of the full-length models in three nucleotide states with the improved model of D2. The rerefinement illustrates both the importance of having high-resolution structures of the constituent domains, as well as several important concepts in low-resolution structure refinement, including the utility of B-factor sharpening, combined phase refinement targets, and improved bulk solvent correction (DeLaBarre and Brunger, 2006; Brunger, 2007). The rerefinement further demonstrates the importance of optimizing these methods to the interpretability of electron density maps in difficult areas.

The revised crystal structures reveal local and remote changes mediated by the interaction of conserved structural motifs with the different nucleotide ligands, and thereby provide a mechanism by which hydrolysis activity is translated into global conformational changes. In particular, pushing of adjacent D2 domains on each other, and transmission of nucleotide state information through the D1-D2 linker to effect displacement of the N domain, appear to drive these changes. Although the nucleotide-dependent changes observed here are well founded in the crystallographic data, orthogonal structural methods, such as SAXS and cryoelectron microscopy, have shown larger conformational changes of p97 as it progresses through the hydrolysis cycle. The limited range of motion of the molecule likely arises from restrictions of the crystal lattice. Nonetheless, the changes in chemical interactions found in the crystal structures are supported by biochemical and other experimental data (Song et al., 2003; Wang et al., 2003a, 2003b; DeLaBarre et al., 2006). Further studies will be needed to understand the relationship between the crystallographically observed chemical differences among nucleotide states and the conformational changes needed to carry out the functions of p97.

EXPERIMENTAL PROCEDURES

Expression and Purification of p97-D2 Domain

The p97-D2 domain (residues 461–806) was expressed with an N-terminal His_6 tag in *Escherichia coli* M15 cells containing the pREP4 plasmid (QIAGEN). The protein was purified by successive passage over Ni^{2+}-NTA Superflow agarose (QIAGEN) and gel filtration columns (Superdex S200 HR26/60; Pharmacia), ending in buffer containing 25 mM Tris (pH 7.5), 150 mM KCl, 5 mM β-mercaptoethanol, 1 mM EDTA, 10% (v/v) glycerol, and 1 mM ATP. Fractions containing pure p97-D2, as determined by SDS-PAGE analysis, were pooled and concentrated to ~20 mg/ml by using Vivaspin 20 spin concentrators with a 10,000 Da molecular weight cutoff (Vivascience).

Crystallization of p97-D2

Crystals of His_6-tagged p97-D2 were obtained by the hanging-drop vapor-diffusion technique. Single crystals of parallelepiped morphology grew from hanging drops set up at 21°C as 2 μl protein solution (20 mg ml^{-1} p97-D2, 25 mM Tris [pH 7.5], 150 mM KCl, 10 mM β-mercaptoethanol, 10 mM $MgCl_2$, and 10 mM ATP-γ-S) mixed with 2 μl reservoir solution (100 mM Tris [pH 7.1], 2.45 M ammonium sulfate, and 0.2 M lithium sulfate). Crystals typically grew in 4–5 days, reaching their maximum dimensions of 75 × 75 × 200 μm^3 in 2 wk. Soaking or growing crystals in the presence of no nucleotide, AMP-PNP, ATP, or ADP produced identical crystals. Individual crystals were

soaked in mother liquor supplemented with 30% (v/v) ethylene glycol and flash frozen in liquid N_2.

Structure Determination of p97-D2

Diffraction data from p97-D2 crystals (Table 1) were collected at 100K on a Q315 CCD detector (λ = 0.98 Å) at beamline 11-1 of the Stanford Synchrotron Radiation Laboratory (Table 1). Data collection revealed that the crystals were of space group C2 and nonisomorphous. Two datasets were used for model building: one with unit cell dimensions of a = 173.3 Å, b = 167.2 Å. c = 209.5 Å, β = 112.3°, with d_{min} = 3.0 Å; and a second with dimensions of a = 172.0 Å, b = 167.2 Å. c = 200.0 Å, β = 110.8°, with d_{min} = 3.8 Å. Both datasets were obtained from crystals grown in the presence of 10 mM ATP-γ-S. Diffraction data were processed with MOSFLM/SCALA. Search models were generated from the D2 portion of PDB ID 1OZ4 (ADP-AlF_x-bound state) (DeLaBarre and Brunger, 2003) and were used for molecular replacement with PHASER (McCoy et al., 2007). Self-rotation analysis with POLARRFN (CCP4, 1994) revealed a broad peak centered at ~51°, corresponding to 7-fold symmetry and confirming the presence of a heptamer. Searches were performed on both data sets with monomers, dimers, trimers, and hexamers found in the crystals of ADP-AlF_x-bound p97, but a clear solution emerged only with the lower-resolution set when four trimers were placed while allowing a significant number of clashes. The resulting map revealed two open rings per asymmetric unit, each with room for insertion of a seventh protomer, for a total of 14 protomers per asymmetric unit. The solvent content with two heptamers per asymmetric unit was 51.0%.

Model Refinement of p97-D2

The model was built in Coot (Emsley and Cowtan, 2004) and refined with CNS v.1.2 (Brunger et al., 1998; Brunger, 2007) with strict 14-fold noncrystallographic symmetry imposed. Due to the high symmetry, a subset of data (10%) was removed in thin shells with DATAMAN (Kleywegt, 1996) before refinement as the test set for crossvalidation. The model was initially refined as two rigid bodies (the α/β subdomain and the α subdomain) subdomain with data from 12–4.0 Å and the MLF target function. The model was rebuilt into a 14-fold averaged map and subjected to sequential rounds of simulated annealing and energy minimization with all data to 3.8 Å. This model was used to phase the higher-resolution dataset and extend phases to 3.0 Å, with subsequent rounds of energy minimization and group B-factor refinement with all data to 3.0 Å. Bulk solvent and anisotropic temperature factor corrections were applied throughout the refinement. Following refinement in CNS, the model was subjected to one final round of TLS refinement with PHENIX (Adams et al., 2002). The noncrystallographic symmetry constraints were dropped once no further improvements could be added to the model, but this did not result in a significant drop in R_{free}, so strict symmetry was maintained in the final model. Final refinement statistics are shown in Table 1.

Rerefinement of Full-Length p97

Structure factors from published structures 1OZ4, 1YQO, 1YPW, and 1YQI (DeLaBarre and Brunger, 2003, 2005) were used and models rerefined with models derived from the union of 1E32 and the newly solved p97-D2 model. Least-squares superposition of the new models to the previously published models was followed by rigid-body refinement. The models were further refined against MLF targets through sequential rounds of energy minimization and group B-factor refinement, with strict noncrystallographic symmetry imposed for all nucleotide states (3-fold for ADP and ADP-AlFx, and 4-fold for ATP). When no further decrease in R factors could be obtained, strict symmetry constraints for the ADP-AlF_x state were dropped in favor of restraints, as previously described (DeLaBarre and Brunger, 2005), and those for the ADP-state NCS symmetry restraints were abandoned altogether, resulting in an improvement in R and R_{free} of ~1%. B-factor sharpening was employed to improve map quality, and models were further refined with the addition of the published experimental MAD phasing data with MLHL target functions (DeLaBarre and Brunger, 2003, 2005). The experimental data for the ADP-AlF_x state were found to be from slightly nonisomorphous crystals, so MAD phases were recomputed with the cell constants from the highest-resolution native dataset for that state. Final refinement statistics are shown in Table 2. For comparison of crystallographic data with models obtained by SAXS, R_g values were calculated from the crystallographic coordinates with the program CRYSOL (Svergun et al., 1995).

ACCESSION NUMBERS

Coordinates and structure factors for p97 D2 and coordinates for the rerefined full-length p97 have been deposited in the Protein Data Bank under ID codes 3CF0 (p97 D2), 3CF2 (p97-AMP-PNP), 3CF1 (p97 ADP-AlFx), and 3CF3 (p97 ADP).

ACKNOWLEDGMENTS

We thank Andy May for performing the initial p97 D2 crystallization screens and for discussions. We thank Wally Whiteheart for generously providing the p97 D2 construct. J.M.D. was supported in part by a National Institutes of Health (NIH) Medical Scientist Training Program grant. Portions of this research were carried out at the Stanford Synchrotron Radiation Laboratory, a national user facility operated by Stanford University on behalf of the U.S. Department of Energy, Office of Basic Energy Sciences. The SSRL Structural Molecular Biology Program is supported by the Department of Energy, Office of Biological and Environmental Research, and by the NIH, National Center for Research Resources, Biomedical Technology Program, and the National Institute of General Medical Sciences. This work was supported by NIH grant MH58570 to W.I.W.

Received: December 4, 2007
Revised: February 11, 2008
Accepted: February 11, 2008
Published: May 6, 2008

REFERENCES

Adams, P.D., Grosse-Kunstleve, R.W., Hung, L.W., Ioerger, T.R., McCoy, A.J., Moriarty, N.W., Read, R.J., Sacchettini, J.C., Sauter, N.K., and Terwilliger, T.C. (2002). PHENIX: building new software for automated crystallographic structure determination. Acta Crystallogr. D Biol. Crystallogr. *58*, 1948–1954.

Beuron, F., Flynn, T.C., Ma, J., Kondo, H., Zhang, X., and Freemont, P.S. (2003). Motions and negative cooperativity between p97 domains revealed by cryo-electron microscopy and quantised elastic deformational model. J. Mol. Biol. *327*, 619–629.

Beyer, A. (1997). Sequence analysis of the AAA protein family. Protein Sci. *6*, 2043–2058.

Brunger, A.T. (2007). Version 1.2 of the Crystallography and NMR system. Nat. Protoc. *2*, 2728–2733.

Brunger, A.T., Adams, P.D., Clore, G.M., Gros, P., Grosse-Kunstleve, R.W., Jiang, J.-S., Kuszewski, J., Nilges, M., Pannu, N.S., Read, R.J., et al. (1998). Crystallography and NMR System (CNS): A new software system for macromolecular structure determination. Acta Crystallogr. D Biol. Crystallogr. *54*, 905–921.

CCP4 (Collaborative Computational Project, Number 4) (1994). The CCP4 suite: programs for protein crystallography. Acta Crystallogr. D Biol. Crystallogr. *50*, 760–763.

Confalonieri, F., and Duguet, M. (1995). A 200-amino acid ATPase module in search of a basic function. Bioessays *17*, 639–650.

Davies, J.M., Tsuruta, H., May, A.P., and Weis, W.I. (2005). Conformational changes of p97 during nucleotide hydrolysis determined by small-angle X-Ray scattering. Structure *13*, 183–195.

DeLaBarre, B., and Brunger, A.T. (2003). Complete structure of p97/valosin-containing protein reveals communication between nucleotide domains. Nat. Struct. Biol. *10*, 856–863.

DeLaBarre, B., and Brunger, A.T. (2005). Nucleotide dependent motion and mechanism of action of p97/VCP. J. Mol. Biol. *347*, 437–452.

DeLaBarre, B., and Brunger, A.T. (2006). Considerations for the refinement of low-resolution crystal structures. Acta Crystallogr. D Biol. Crystallogr. *62*, 923–932.

DeLaBarre, B., Christianson, J.C., Kopito, R.R., and Brunger, A.T. (2006). Central pore residues mediate the p97/VCP activity required for ERAD. Mol. Cell *22*, 451–462.

Dreveny, I., Kondo, H., Uchiyama, K., Shaw, A., Zhang, X., and Freemont, P.S. (2004). Structural basis of the interaction between the AAA ATPase p97/VCP and its adaptor protein p47. EMBO J. *23*, 1030–1039.

Emsley, P., and Cowtan, K. (2004). Coot: Model-building tools for molecular graphics. Acta Crystallogr. D Biol. Crystallogr. *60*, 2126–2132.

Fleming, K.G., Hohl, T.M., Yu, R.C., Müller, S.A., Wolpensinger, B., Engel, A., Engelhardt, H., Brunger, A.T., Söllner, T.H., and Hanson, P.I. (1998). A revised model for the oligomeric state of the N-ethylmaleimide-sensitive fusion protein, NSF. J. Biol. Chem. *273*, 15675–15681.

Gai, D., Zhao, R., Li, D., Finkielstein, C.V., and Chen, X.S. (2004). Mechanisms of conformational change for a replicative hexameric helicase of SV40 large tumor antigen. Cell *119*, 47–60.

Hanson, P.I., Roth, R., Morisaki, H., Jahn, R., and Heuser, J.E. (1997). Structure and conformational changes in NSF and its membrane receptor complexes visualized by quick-freeze/deep-etch electron microscopy. Cell *90*, 523–535.

Hitchcock, A.L., Krebber, H., Frietze, S., Lin, A., Latterich, M., and Silver, P.A. (2001). The conserved npl4 protein complex mediates proteasome-dependent membrane-bound transcription factor activation. Mol. Biol. Cell *12*, 3226–3241.

Huyton, T., Pye, V.E., Briggs, L.C., Flynn, T.C., Beuron, F., Kondo, H., Ma, J., Zhang, X., and Freemont, P.S. (2003). The crystal structure of murine p97/VCP at 3.6A. J. Struct. Biol. *144*, 337–348.

Karata, K., Inagawa, T., Wilkinson, A.J., Tatsuta, T., and Ogura, T. (1999). Dissecting the role of a conserved motif (the second region of homology) in the AAA family of ATPases. Site-directed mutagenesis of the ATP-dependent -protease FtsH. J. Biol. Chem. *274*, 26225–26232.

Kleywegt, G.J., and Jones, T.A. (1996). xdlMAPMAN and xdlDATAMAN— programs for reformatting, analysis and manipulation of biomacromolecular electron-density maps and reflection data sets. Acta Crystallogr. D Biol. Crystallogr. *52*, 826–828.

Kondo, H., Rabouille, C., Newman, R., Levine, T.P., Pappin, D., Freemont, P., and Warren, G. (1997). p47 is a cofactor for p97-mediated membrane fusion. Nature *388*, 75–78.

Laskowski, R.A., MacArthur, M.W., Moss, D.S., and Thornton, J.M. (1993). PROHECK: a program to check the steroechemical quality of protein structures. J. Appl. Crystallogr. *26*, 283–291.

Lee, S.Y., De La Torre, A., Yan, D., Kustu, S., Nixon, B.T., and Wemmer, D.E. (2003). Regulation of the transcriptional activator NtrC1: structural studies of the regulatory and AAA^+ ATPase domains. Genes Dev. *17*, 2552–2563.

Lupas, A.N., and Martin, J. (2002). AAA proteins. Curr. Opin. Struct. Biol. *12*, 746–753.

Matveeva, E.A., May, A.P., He, P., and Whiteheart, S.W. (2002). Uncoupling the ATPase activity of the N-ethylmaleimide sensitive factor (NSF) from 20S complex disassembly. Biochemistry *41*, 530–536.

McCoy, A.J., Grosse-Kunstleve, R.W., Adams, P.D., Winn, M.D., Storoni, L.C., and Read, R.J. (2007). Phaser crystallographic software. J. Appl. Crystallorg. *40*, 658–674.

Meyer, H.H., Shorter, J.G., Seemann, J., Pappin, D., and Warren, G. (2000). A complex of mammalian ufd1 and npl4 links the AAA-ATPase, p97, to ubiquitin and nuclear transport pathways. EMBO J. *19*, 2181–2192.

Neuwald, A.F., Aravind, L., Spouge, J.L., and Koonin, E.V. (1999). AAA^+: a class of chaperone-like ATPases assoicated with the assembly, operation, and disassembly of protein complexes. Genome Res. *9*, 27–43.

Niwa, H., Tsuchiya, D., Makyio, H., Yoshida, M., and Morikawa, K. (2002). Hexameric ring structure of the ATPase domain of the membrane-integrated metalloprotease FtsH from Thermus thermophilus HB8. Structure *10*, 1415–1423.

Ogura, T., and Wilkinson, A.J. (2001). AAA^+ superfamily ATPases: common structure-diverse function. Genes Cells *6*, 575–597.

Patel, S., and Latterich, M. (1998). The AAA team: related ATPases with diverse functions. Trends Cell Biol. *8*, 65–71.

Peters, J.-M., Harris, J.R., Lustig, A., Müller, S., Engel, A., Volker, S., and Franke, W.W. (1992). Ubiquitous soluble Mg^{2+}-ATPase complex: a structural study. J. Mol. Biol. *223*, 557–571.

Rabinovich, E., Kerem, A., Frohlich, K.U., Diamant, N., and Bar-Nun, S. (2002). AAA-ATPase p97/Cdc48p, a cytosolic chaperone required for endoplasmic reticulum-associated protein degradation. Mol. Cell. Biol. *22*, 626–634.

Rockel, B., Walz, J., Hegerl, R., Peters, J., Typke, D., and Baumeister, W. (1999). Structure of VAT, a CDC48/p97 ATPase homologue from the archeon *Thermoplasma acidophilum* as studied by electron tomography. FEBS Lett. *451*, 27–32.

Rosenberg, O.S., Deindl, S., Sung, R.J., Nairn, A.C., and Kuriyan, J. (2005). Structure of the autoinhibited kinase domain of CaMKII and SAXS analysis of the holoenzyme. Cell *123*, 849–860.

Rosenberg, O.S., Deindl, S., Comolli, L.R., Hoelz, A., Downing, K.H., Nairn, A.C., and Kuriyan, J. (2006). Oligomerization states of the association domain and the holoenzyme of Ca^{2+}/CaM kinase II. FEBS J. *273*, 682–694.

Rouiller, I., Butel, V.M., Latterich, M., Milligan, R.A., and Wilson-Kubalek, E.M. (2000). A Major Conformational Change in p97 AAA ATPase upon ATP binding. Mol. Cell *6*, 1485–1490.

Rouiller, I., DeLaBarre, B., May, A.P., Weis, W.I., Brunger, A.T., Milligan, R.A., and Wilson-Kubalek, E.M. (2002). Conformational changes of the multifunction p97 AAA ATPase during its ATPase cycle. Nat. Struct. Biol. *9*, 950–957.

Song, C., Wang, Q., and Li, C.C. (2003). ATPase activity of p97-valosin-containing protein (VCP). D2 mediates the major enzyme activity, and D1 contributes to the heat-induced activity. J. Biol. Chem. *278*, 3648–3655.

Sousa, M.C., Trame, C.B., Tsuruta, H., Wilbanks, S.M., Reddy, V.S., and McKay, D.B. (2000). Crystal and solution structures of an HslUV protease-chaperone complex. Cell *103*, 633–643.

Suno, R., Niwa, H., Tsuchiya, D., Zhang, X., Yoshida, M., and Morikawa, K. (2006). Structure of the whole cytosolic region of ATP-dependent protease FtsH. Mol. Cell *22*, 575–585.

Svergun, D., Barberato, C., and Koch, M.H.J. (1995). CRYSOL: a program to evaluate X-ray solution scattering of biological macromolecules from atomic coordinates. J. Appl. Crystallogr. *28*, 768–773.

Uchiyama, K., and Kondo, H. (2005). p97/p47-Mediated biogenesis of Golgi and ER. J. Biochem. (Tokyo) *137*, 115–119.

Vale, R.D. (2000). AAA proteins. Lords of the ring. J. Cell Biol. *150*, F13–F19.

Wang, J., Song, J.J., Seong, I.S., Franklin, M.C., Kamtekar, S., Eom, S.H., and Chung, C.H. (2001). Nucleotide-dependent conformational changes in a protease-associated ATPase HslU. Structure *9*, 1107–1116.

Wang, Q., Song, C., and Li, C.C. (2003a). Hexamerization of p97-VCP is promoted by ATP binding to the D1 domain and required for ATPase and biological activities. Biochem. Biophys. Res. Commun. *300*, 253–260.

Wang, Q., Song, C., Yang, X., and Li, C.C. (2003b). D1 ring is stable and nucleotide-independent, whereas D2 ring undergoes major conformational changes during the ATPase cycle of p97-VCP. J. Biol. Chem. *278*, 32784–32793.

Ye, Y., Meyer, H.H., and Rapoport, T.A. (2001). The AAA ATPase Cdc48/p97 and its partners transport proteins from the ER into the cytosol. Nature *414*, 652–656.

Zhang, X., Shaw, A., Bates, P.A., Newman, R.H., Gowen, B., Orlova, E., Gorman, M.A., Kondo, H., Dokurno, P., Lally, J., et al. (2000). Structure of the AAA ATPase p97. Mol. Cell *6*, 1473–1484.

